ARTICLE IN PRESS

Nano Materials Science xxx (xxxx) xxx

Contents lists available at ScienceDirect

Nano Materials Science

journal homepage: www.keaipublishing.com/cn/journals/nano-materials-science/

Synergy of compress strain and antioxidant of platinum-copper for enhanced the oxygen reduction performance

Jun Zhang [a,*], Pingjuan Liang [b], Xinlan Xu [b], Rong Wang [a], Shuyue Liu [a], Chunyuan Wang [b], Boyu Liu [b], Laizheng Luo [c], Meng Jin [a], Huan Liu [d], Huan Yi [b], Shi-Yu Lu [a,**]

[a] College of Metallurgy and Materials Engineering, Chongqing University of Science and Technology, Chongqing, 401331, China
[b] College of Chemistry and Chemical Engineering, Chongqing University of Science and Technology, Chongqing, 401331, China
[c] Southwest Technology and Engineering Research Institute, Chongqing, 400039, China
[d] School of Physical and Mathematical Sciences, Nanyang Technological University, Singapore, 637371, Singapore

ARTICLE INFO

Keywords:
PtCu alloy
Compressive strain
Oxygen reduction reaction
Activity and durability
Cu oxidation

ABSTRACT

The development of efficient and durable electrocatalysts for oxygen reduction reaction (ORR) holds a pivotal significance in the successful commercialization of proton exchange membrane fuel cells (PEMFCs) but is still challenging. Herein, we report a worm-liked PtCu nanocrystals dispersed on nitrogen-doped carbon hollow microspheres ($Pt_{0.38}Cu_{0.62}$/N-HCS). Benefiting from its structural and compositional advantages, the resulting $Pt_{0.38}Cu_{0.62}$/N-HCS catalyst delivers exceptional electrocatalytic activity for ORR, with a half-wave potential ($E_{1/2}$) of 0.837 V, a mass activity of 0.672 A mg_{Pt}^{-1}, and a Tafel slope of 50.66 mV dec^{-1}, surpassing that of commercial Pt/C. Moreover, the $Pt_{0.38}Cu_{0.62}$/N-HCS follows the desired four-electron transfer mechanism throughout the ORR process, thereby displaying a high selectivity for direct reduction of O_2 to H_2O. Remarkably, this catalyst also showcases high stability, with only a 25 mV drop in $E_{1/2}$ after 10,000 cycles in an acidic electrolyte. Theoretical calculations elucidate the incorporation of Cu into Pt lattice induces compressive strain, which effectively tailors the d band center of Pt active sites and strengthens the surface chemisorption of O_2 molecules on PtCu alloys. Consequently, the $Pt_{0.38}Cu_{0.62}$/N-HCS catalyst exhibits an improved ability to adsorb O_2 molecules on its surface, accelerating the reaction kinetics of O_2 conversion to *OOH. Additionally, Cu atoms, not only serving as sacrificial anode, undergo preferential oxidation during PEMFCs operation when compared to Pt, but also the stable Cu species in PtCu alloys contributes significantly to maintaining the strain effect, collectively enhancing both activity and durability. Overall, this research offers an effective and promising approach to enhance the activity and stability of Pt-based ORR electrocatalysts in PEMFCs.

1. Introduction

Due to their zero carbon emissions and high energy conversion, proton exchange membrane fuel cells (PEMFCs), as a promising sustainable energy conversion technology, have garnered significant attention in various applied fields [1–3]. Currently, the dominant use of noble Platinum (Pt) exhibits superior kinetic activity for oxygen reduction reaction (ORR) throughout a four-electron transfer process. However, the high cost, limited reserves, and poor durability have severely hindered the large-scale commercial application of Pt-based PEMFCs [4,5]. Therefore, it is an urgent need for the development of highly efficient and low-Pt catalysts to improve the performance of ORR [6–10].

Alloying Pt with 3d transition metals have been emerged as an efficient strategy to greatly reduce Pt dosage and improve ORR performance [11–17]. PtFe, PtCo, and PtNi nanoalloys are the promising ORR catalysts with high activity, however, they suffer from severe leaching/dissolution in acidic or corrosive environments for the accelerated degradation tests (ADT), greatly limiting the durability of the membrane electrode assembly [18,19]. Cu^{2+}/Cu exhibits a significantly more positive anodic potential (0.3 V vs. Reversible hydrogen electrode (RHE)) compared to Fe^{2+}/Fe (-0.5 V), Co^{2+}/Co (-0.2 V), and Ni^{2+}/Ni (0.1 V), which suggests that Cu demonstrates magnificent candidate for Pt-based alloying with greater stability and resistance to dissolution in the electrochemical conditions. The electronic structure of Pt can be optimized by 3d

---

* Corresponding author.
** Corresponding author.
E-mail addresses: junzhang@cqust.edu.cn (J. Zhang), lushiyu@cqust.edu.cn (S.-Y. Lu).

https://doi.org/10.1016/j.nanoms.2024.02.011

Please cite this article as: J. Zhang et al., Synergy of compress strain and antioxidant of platinum-copper for enhanced the oxygen reduction performance, Nano Materials Science , https://doi.org/10.1016/j.nanoms.2024.02.011

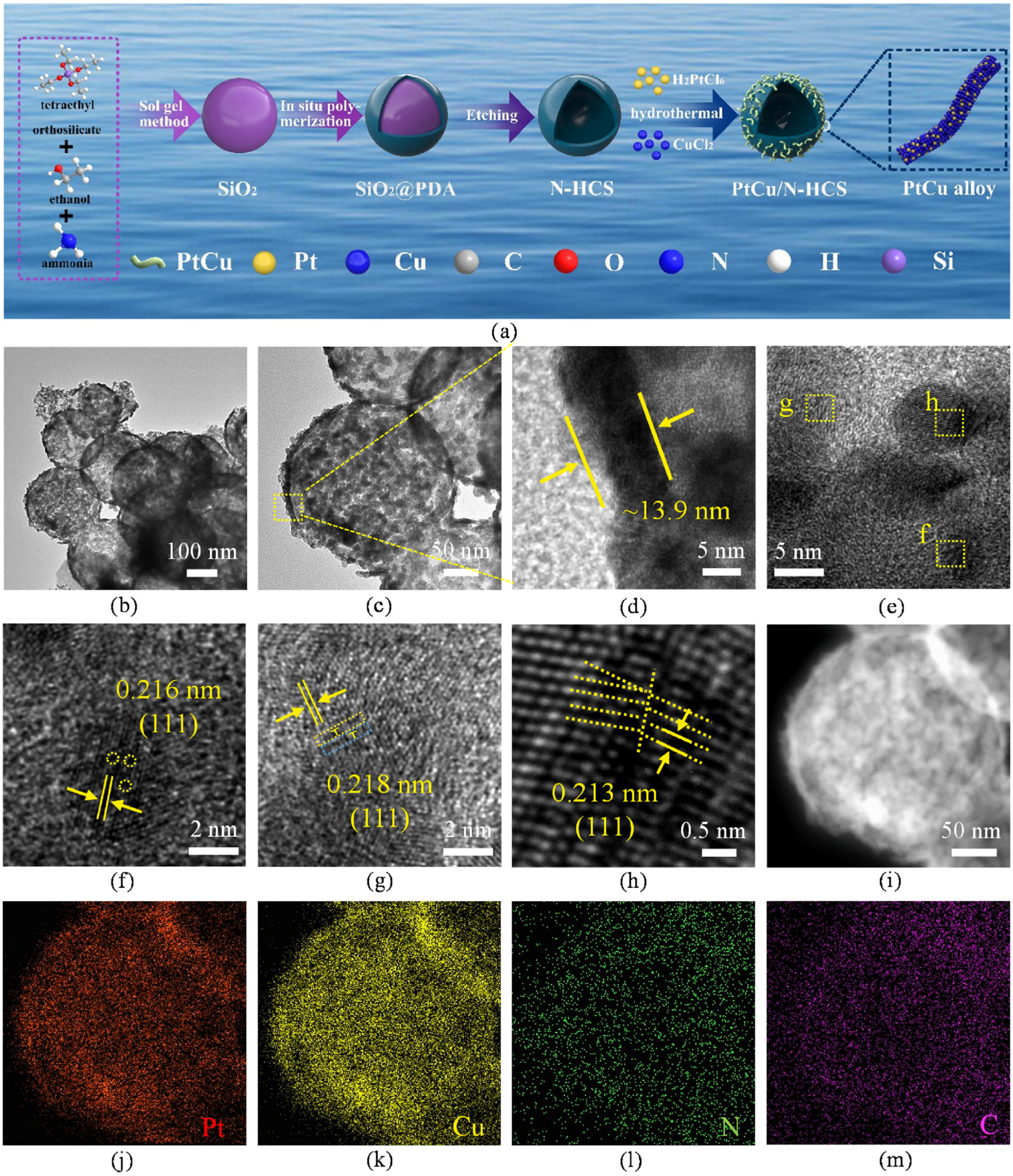

Fig. 1. (a) Schematic diagram of synthesize PtCu/N-HCS materials. (b-c) TEM, (d) yellow boxed portion of (c), (e) HR-TEM image, (f) point defects, (g) line defects (edge dislocation), and (h) plane defects (small-angle grain boundaries), (i-m) HAADF-STEM images and elemental mapping results of $Pt_{0.38}Cu_{0.62}$/N-HCS.

transition metals through the strain and ligand effects, optimizing the adsorption strength of oxygenated intermediates and leading to boosting the electrocatalytic performance of PtM electrocatalysts. The phenomenon of A lattice mismatch occurs when two elements with different lattice parameters contact in directly, which leads to lattice distortion (i.e. lattice strain) in each crystalline component. The strain effect on the reactivity of metal surfaces has been attributed to that the d-bands center of metal approach to Fermi level, which optimize the adsorption energy strengths of oxygen molecules [20]. On the other hand, Pt-based catalyst inevitable display poor durability when exposed to high potentials greater than 0.85 V and lower pH levels below 2 in PEMFCs operation, where is the cathode catalysts for ORR are employed [21]. In such harsh conditions, metallic Pt^0 undergoes oxidation, leading to the formation of Pt^{2+} ions and the reduction in size and disappearance of Pt nanoparticles, resulting in the electrochemical surface area (ECSA) decrease and the half-wave potential ($E_{1/2}$) negatively shifts, which caused rapid decline on ORR performance [22–25]. Despite of numerous efforts devoted to enhance either the catalytic performance or the stability of Pt, together improvement of catalytic activity and stability for Pt-based catalysts remains a huge challenge. Furthermore, the underlying mechanism of the increasement remains murky. As a suitable electrocatalyst support material, nitrogen-doped hollow carbon materials have garnered considerable attention in fuel cells, owing to their high specific surface area and ordered porous structure [26]. Generally, nitrogen-doped hollow carbon significantly enhances the catalyst activity and durability due to the following advantages: 1) The substantial surface area facilitates metal

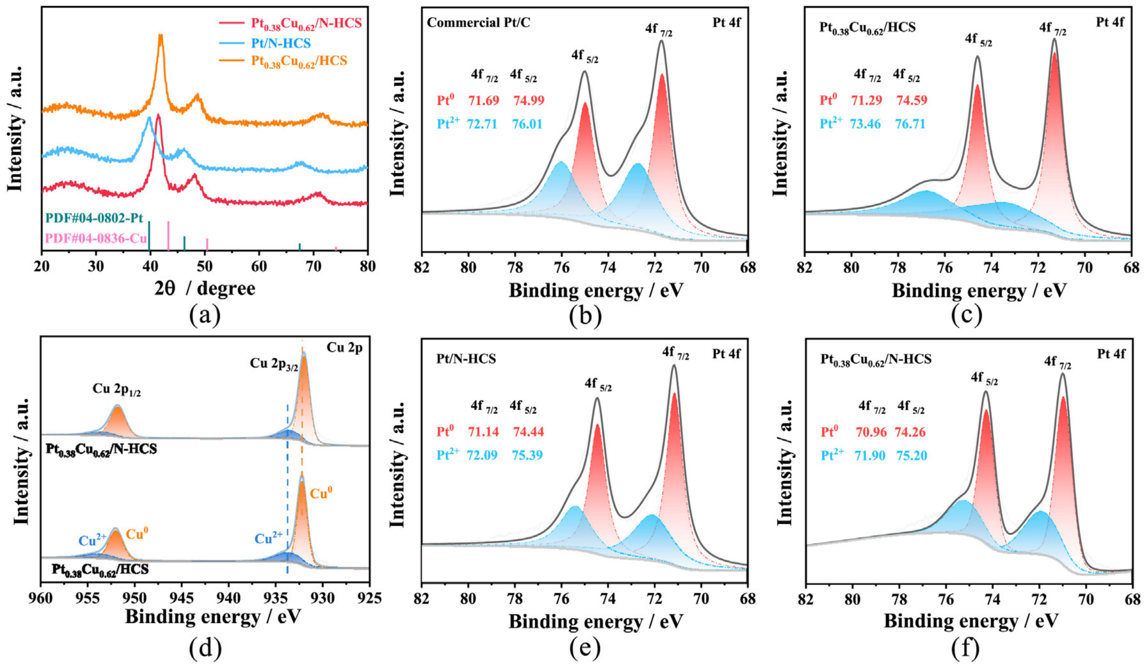

Fig. 2. (a) XRD pattern of $Pt_{0.38}Cu_{0.62}$/N-HCS, Pt/N-HCS and $Pt_{0.38}Cu_{0.62}$/HCS. (b-c and e-f) The Pt 4f XPS spectra of Commercial Pt/C, $Pt_{0.38}Cu_{0.62}$/N-HCS, Pt/N-HCS and $Pt_{0.38}Cu_{0.62}$/HCS, (d) The Cu 2p XPS spectra of $Pt_{0.38}Cu_{0.62}$/N-HCS, $Pt_{0.38}Cu_{0.62}$/HCS.

nanoparticles deposition, maximizing the active sites utilization [27]; 2) The strong metal-support interactions benefit to anchor Pt nanoparticles on the nitrogen-doped carbon support [28]; 3) The favorable macro/meso-porous structure promotes active site exposure and efficient mass transfer [29]; 4) Nitrogen atoms regulate charge redistribution among carbon atoms, enhancing the electron mobility and optimizing the catalytic activity towards ORR [30].

Based on above consideration, we present robust and efficient ORR catalysts composed of worm-like PtCu alloys loaded on nitrogen-doped hollow carbon spheres (Pt_xCu_y/N-HCS). The N-HCS support features a hollow sphere structure with a thin shell and a large specific surface area, facilitating the uniform distribution of PtCu nanoparticles and enabling rapid interfacial charge and mass transfer. Furthermore, the incorporation of Cu atoms into Pt lattice optimizes the electronic structure of PtCu, enhancing the oxygen adsorption. Consequently, $Pt_{0.38}Cu_{0.62}$/N-HCS achieves a positive $E_{1/2}$ of 0.837 V, a mass activity of 0.672 A mg_{Pt}^{-1} and faster reaction kinetic toward ORR compared to commercial Pt/C catalyst. Moreover, the $Pt_{0.38}Cu_{0.62}$/N-HCS catalyst delivers a four-electron ORR mechanism and outstanding stability, with only a 25 mV drop in $E_{1/2}$ after 10000 cycles within the potential range of 0.05-1.2 V. Theoretical calculations reveals that the compress strain in PtCu alloy effectively modifies the electronic structure of Pt sites and drives the density of states of Pt atoms near the Fermi level, resulting in an enhancement for O_2 adsorption on the PtCu (111) surface, thereby improving ORR catalytic activity. Additionally, the improved stability of $Pt_{0.38}Cu_{0.62}$/N-HCS after ADT is attributed to the preferential oxidation of Cu atoms relative to Pt atoms when Cu acts as a sacrificial anode and the intrinsic excellent stability of Cu atoms under acidic conditions. This work provides a promising approach to the design of highly efficient and durable low-Pt catalysts for PEMFCs.

2. Results and discussion

The synthesis of PtCu/N-HCS involves the following steps (Fig. 1a). Firstly, SiO_2 was first obtained by sol-gel method. Then, SiO_2@PDA was obtained after in-situ polymerization and further carbonized at high temperature to obtain SiO_2@NC. Finally, PtCu alloy was loaded on the N-HCS etched from SiO_2@NC. From scanning electron microscopy (SEM) images (Fig. S1), the solid SiO_2@PDA sphere were distributed uniformly with average diameter of 161.5 nm. After calcination, the mean diameter of SiO_2@N-CS (~156.2 nm) slightly smaller than that of SiO_2@PDA, owing to shrinkage of decomposition of organic matter to form N-doped carbon at high temperature (Fig. S2). After etching process, SiO_2 was removed from the interior of the SiO_2@N-HCS, thus a hollow spherical structure of N-HCS were formed (Fig. S3). Due to condensation of the hollow spherical thin shell after etching, the particle size of N-HCS was significantly reduced (~149.2 nm) (Fig. S4). Brunauer-Emmett-Teller (BET) surface area of N-HCS was about 196.7 m^2 g^{-1}, and the aperture distribution was ~11 nm (Fig. S5). Owing to its abundant anchoring sides, high specific surface area and great electron transport ability, hollow and porous N-doped carbon sphere served as an ideal support for catalyst, which was able to improve the electrocatalytic performance of ORR. For comparison, hollow carbon spheres without N-doping were also prepared through the leaching of the annealed SiO_2@C spheres, denoted as HCS (Fig. S6). As depicted in Fig. S7, a type-IV isotherms featuring distinct hysteresis loops within the range of $P/P_0 = 0.5$-1.0 was observed, and the average pore size distribution was approximately 4 nm, both evidenced the existence of mesoporous structure in HCS. The enlarged pore size distribution in N-HCS proves advantageous for anchoring PtCu alloys onto its surface, which facilitating the uniform and high-density loading of PtCu nanoparticles and enhancing the strong metal-support interactions, thus improving the ORR performance.

Due to the above promising properties of N-HCS, structures of $Pt_{0.38}Cu_{0.62}$/N-HCS were characterized in detail by transmission electron microscopy (TEM). The worm-liked PtCu alloys were uniform and highly dense distributed on the hollow spherical N-HCS (Fig. 1b and c), which showed the average size of ~33.9 nm and 10.3 nm in length and width, respectively (Fig. S8), the wall thickness of the N-HCS support was about 13.9 nm (Fig. 1d). The selected area electron diffraction (SAED) pattern further confirmed the presence of (111), (200) and (220) plane of *fcc*-PtCu (Fig. S9). The TEM images of Pt/N-HCS (Fig. S10) exhibited that high dense small Pt nanoparticles evenly dispersed on the surface of N-HCS. However, the TEM images of $Pt_{0.38}Cu_{0.62}$/HCS (Fig. S11) showed that scattered a little of PtCu nanoparticles dispersed on the HCS. It was worth noting that the d-spacing of (111) plane in *fcc*-Pt was obviously larger than that of *fcc*-PtCu alloy, indicating existence of compressive

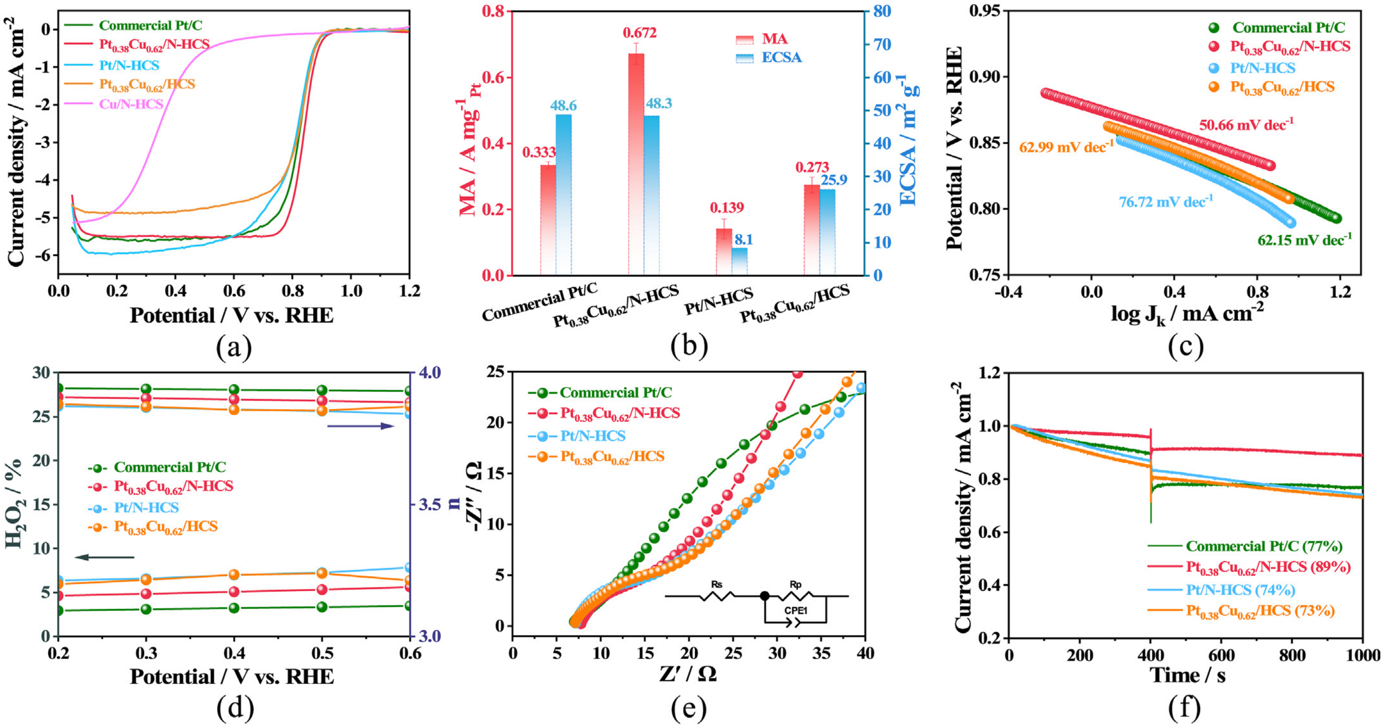

(a) (b) (c)

(d) (e) (f)

Fig. 3. (a) LSV for Commercial Pt/C, $Pt_{0.38}Cu_{0.62}$/N-HCS, Pt/N-HCS and $Pt_{0.38}Cu_{0.62}$/HCS catalysts in 0.1 M $HClO_4$. (b) Mass activity (MA) and ECSA. (c) Corresponding Tafel plots; (d) Electron transfer number and H_2O_2 yield; (e) Electrochemical impedance spectroscopy curves; (f) Methanol crossover resistance.

strain in PtCu alloy. The HR-TEM images of PtCu clearly presented the structural remodeling (point defects, surface defects) and the lattice of PtCu was obviously compressed (Fig. 1e-h). The lattice spacing of 0.213 nm-0.218 nm corresponded to the Pt (111) surface, indicating the presence of compressive strain [31,32]. The formation of defects caused a compressive strain on the Pt lattice, and the compressive strain reduces the vacancy formation energy, which favors defect generation. The elements Pt, Cu, N and C are uniformly distributed throughout the nano-alloys (Fig. 1i-m).

The X-ray diffraction (XRD) patterns of $Pt_{0.38}Cu_{0.62}$/N-HCS (Fig. 2a) revealed a highly crystalline *fcc* phase and a notable shift towards higher degrees when compared to pure Pt (PDF#04-0802). This shift unequivocally confirmed the well-alloyed structure and contracted lattice spacing in $Pt_{0.38}Cu_{0.62}$/N-HCS. Furthermore, the most robust (111) peak intensity in $Pt_{0.38}Cu_{0.62}$/N-HCS, $Pt_{0.38}Cu_{0.62}$/HCS and Pt/N-HCS verified the preferential orientation within both N-HCS and HCS. Interestingly, as the Cu atom content increased, the Pt_xCu_y peaks shifted towards higher angles (Fig. S12), which may be attributed to compressive strain caused by the incorporation of Cu atoms into the Pt lattice [33,34]. To gain insight into the surface composition and chemical status of the catalysts, X-ray photoelectron spectroscopy (XPS) was also employed. The survey-level spectrum (Fig. S13, Table S2) confirms the presence of Cu, Pt, C and N in $Pt_{0.38}Cu_{0.62}$/N-HCS. In comparison, no signal of Cu is detected in Pt/N-HCS and Pt/C, while no signal of N is observed in $Pt_{0.38}Cu_{0.62}$/HCS and Pt/C [35].

In Fig. 2b-c and 2e-2f, the Pt 4f orbitals indicated the presence of Pt species predominantly in a metallic state across all catalysts [36]. Remarkably, when compared to commercial Pt/C, $Pt_{0.38}Cu_{0.62}$/HCS, Pt/N-HCS and $Pt_{0.38}Cu_{0.62}$/N-HCS, the $Pt_{0.38}Cu_{0.62}$/N-HCS catalyst exhibited the highest proportion of the metallic state (Table S3), which could significantly accelerate the ORR reaction kinetic [37,38]. To investigate the impact of Cu atom on the electronic structure of Pt, the binding energy of Pt $4f_{7/2}$ spectra was analyzed before and after the addition of Cu atoms. As shown in Fig. 2b-c, 2e-2f, the binding energy of Pt $4f_{7/2}$ peaks (71.29 eV) on $Pt_{0.38}Cu_{0.62}$/HCS undergoes a negative shift of 0.4 eV in comparison to that of commercial Pt/C (71.69 eV). Similarly, the Pt $4f_{7/2}$ peaks of $Pt_{0.38}Cu_{0.62}$/N-HCS (70.96 eV) exhibited a lower binding energy when compared with Pt/N-HCS (71.14 eV) [39]. These negative shifts in Pt peaks could be attributed to the strong electron interactions between Pt and Cu, which favored the ORR activity following the incorporation of Cu atoms into the Pt lattice. Furthermore, in generally, the loss of electrons by an element tends to induce an upward shift in its binding energy towards a higher field, whereas the obtain of electrons results in a downward shift towards a lower field in its binding energy. This electron migration process elucidates the interactions among elements. Doping heteroatoms in the carbon substrate can change the charge distribution and electronic properties of the carbon layer, providing a stronger interaction between the ORR active center and the heteroatom-doped carbon layer, thus improving the catalytic activity and stability [40]. The influence of N-doping on the electronic structure of Pt and Cu atoms was also investigated by XPS. The Pt $4f_{7/2}$ of Pt/N-HCS (Fig. 2e) shifted negatively by 0.55 eV compared with commercial Pt/C (Fig. 2b), while Pt $4f_{7/2}$ of $Pt_{0.38}Cu_{0.62}$/N-HCS (Fig. 2f) exhibited a negative shift of 0.33 eV relative to $Pt_{0.38}Cu_{0.62}$/HCS (Fig. 2c) [41]. Accordingly, the Cu $2p_{3/2}$ of $Pt_{0.38}Cu_{0.62}$/N-HCS shifted negatively by 0.17 eV in contrast to $Pt_{0.38}Cu_{0.62}$/HCS (Fig. 2d and Table S4). Furthermore, the electronic structure of Pt and Cu atoms was also influenced by N-doping [42]. These results collectively point to an electron transfer from N species to neighboring Pt and Cu atoms, optimizing the d-band center of PtCu and thereby enhancing oxygen adsorption. Additionally, compared with Pt/N-HCS, alloyed Cu atoms reduced the content of pyrrolic-N and significantly increased the combined contents of pyridinic-N and graphitic-N (Fig. S14 and Table S5) [43,44]. The spectrum of C 1s divided into four characteristic peaks located at 284.5, 284.9, 285.6, and 286.5 eV, which attributed to C=C, C-C, C-N/C-O, and C=O bonds, respectively (Fig. S15 and Table S6) [26]. The Cu and Pt atoms in $Pt_{0.38}Cu_{0.62}$/N-HCS were predominantly in the metallic state, and a strong peak shifted signifies a significant alteration in the surface electronic structure of $Pt_{0.38}Cu_{0.62}$/HCS. This shift originated from the charge transfer from Cu to Pt, culminating in optimized adsorption for reaction intermediate on the surface of PtCu alloys [45].

To assess how the atomic ratios of PtCu alloy influence ORR

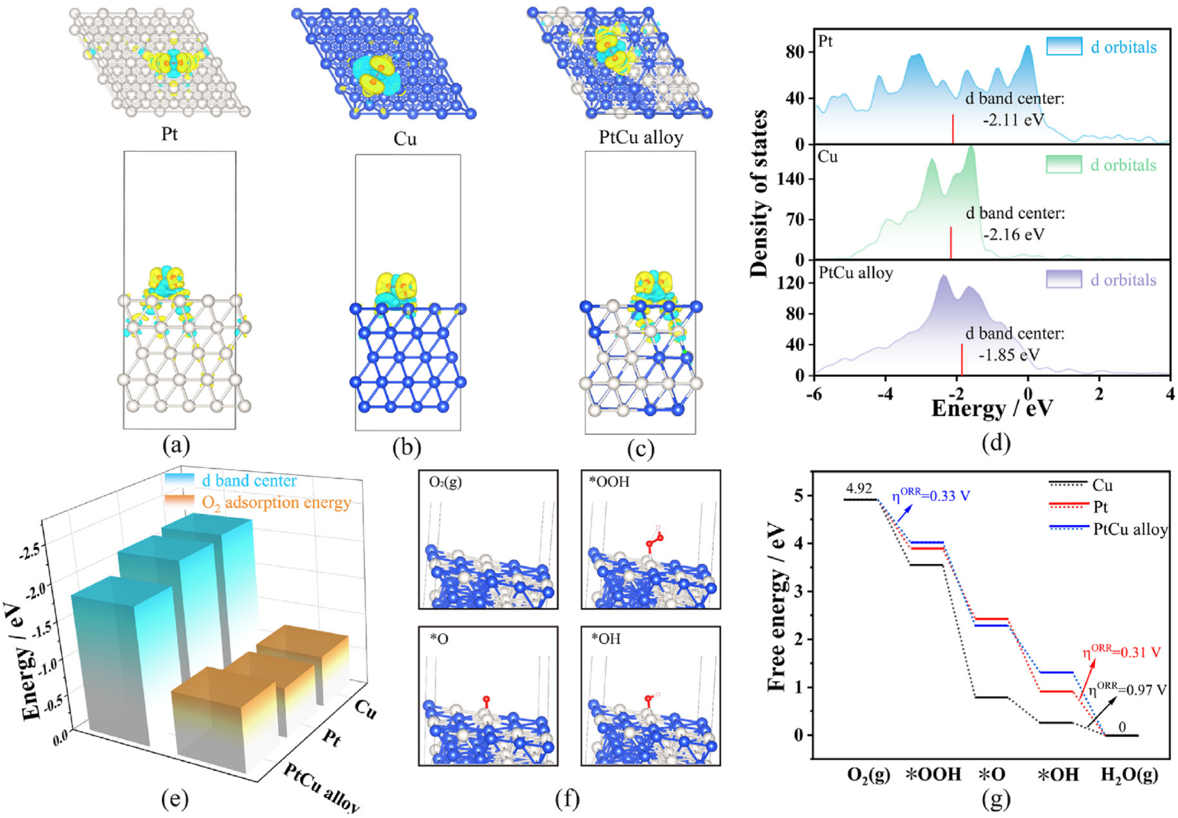

Fig. 4. The three-dimensional charge density difference of O_2 adsorbed on Pt (111) (a), Cu (111) (b), and PtCu (111) (c) with an isovalue of 0.0018 e/Bohr^3. The yellow and cyan areas indicate electron accumulation and depletion, respectively; (d) PDOS of d-bands of Cu (111), Pt (111), and PtCu (111); (e) Calculated d band center and O_2 adsorption energy for Cu (111), Pt (111), and PtCu (111); (f) ORR pathway with the most energetically favorable absorbed intermediates (*OOH, *O, *OH) in PtCu (111); (g) Free-energy diagram for the ORR on Cu (111), Pt (111), and PtCu (111) at zero electrode potential.

performance, we conducted CV and LSV curve analyses of Pt_xCu_y catalysts using the rotating disk electrode method. When N_2-saturated 0.1 M $HClO_4$ electrolytes, the Pt_xCu_y catalyst displayed a rectangular shape, while presented a distinct cathodic reduction peak under O_2 conditions (Fig. S16a). This observation indicated that all Pt_xCu_y catalysts demonstrated excellent ORR activity. In general, LSV curves obtained at various rotation rates provide insights into the kinetic and catalytic pathways for ORR. In Fig. S16b, the onset potential (E_{onset}) of each catalyst remained relatively stable, while the diffusion-limited current density (J_L) increased significantly at higher rotational speeds, inferring enhanced mass transfer behavior at higher speeds. We evaluated the ORR activities of Pt_xCu_y catalysts based on E_{onset} and $E_{1/2}$. As depicted in Fig. S17a and Table S7, the Pt_xCu_y catalysts achieved their maximum ORR activity when the atomic ratio is 0.38/0.62 (0.998 V and 0.837 V for E_{onset} and $E_{1/2}$, respectively). Furthermore, to further investigate the ORR catalytic performance, the mass activity (MA) was calculated by normalizing current density against Pt loading in catalyst, and the electrochemically active surface area (ECSA) was determined based on CO-stripping (Fig. S18). As shown in Fig. S17b, the MA and ECSA of Pt_xCu_y catalysts followed a similar volcano-shaped distribution as the Cu content increased. Notably, the $Pt_{0.38}Cu_{0.62}$/N-HCS catalyst displayed the highest MA of 0.672 A mg$^{-1}_{Pt}$, ECSA of 48.3 m^2 g^{-1}. The Tafel slope, obtained from LSV curves, served as a crucial descriptor for ORR kinetics. As indicated in Fig. S17c, the $Pt_{0.38}Cu_{0.62}$/N-HCS catalyst exhibited the smallest Tafel slopes compared to the $Pt_{0.29}Cu_{0.71}$/N-HCS and $Pt_{0.44}Cu_{0.56}$/N-HCS catalysts. Based on the aforementioned analysis, it was evident that the atomic ratios between Pt and Cu atoms play a crucial role in regulating compressive strain, which optimizes the O_2 adsorption ability on the PtCu (111) surface. Therefore, the $Pt_{0.38}Cu_{0.62}$/N-HCS catalyst is selected for further study on ORR performance.

To assess the superior performance of $Pt_{0.38}Cu_{0.62}$/N-HCS for ORR, the electrochemical tests were carried out on Pt/N-HCS, $Pt_{0.38}Cu_{0.62}$/HCS, and commercial Pt/C in N_2 and O_2-saturated 0.1 M $HClO_4$ electrolyte (Fig. S19). In Fig. 3a, it was evident that $Pt_{0.38}Cu_{0.62}$/N-HCS exhibited the most positive $E_{1/2}$ of 0.837 V when compared to commercial Pt/C (0.822V), Pt/N-HCS (0.807V) and $Pt_{0.38}Cu_{0.62}$/HCS (0.827V). Benefiting from the well-controlled strain in catalyst, the $Pt_{0.38}Cu_{0.62}$/N-HCS also presented highest MA of 0.672 A mg$^{-1}_{Pt}$, which was 2.0, 4.8, and 2.5 times greater than those of commercial Pt/C (0.333 A mg$^{-1}_{Pt}$), Pt/N-HCS (0.139 A mg$^{-1}_{Pt}$) and $Pt_{0.38}Cu_{0.62}$/HCS (0.273 A mg$^{-1}_{Pt}$) catalysts, respectively (Fig. 3b, Table S8). These results clearly indicate the optimized electronic structure of Pt by Cu-induced compressive strain [46]. Similarly, the electrochemically active surface area (ECSA) was determined based on CO-stripping (Fig. S20). The ECSA of $Pt_{0.38}Cu_{0.62}$/N-HCS (48.3 m^2 g^{-1}) is comparable to that of commercial Pt/C (48.6 m^2 g^{-1}) and surpassed that of Pt/N-HCS (8.1 m^2 g^{-1}) and $Pt_{0.38}Cu_{0.62}$/HCS (25.9 m^2 g^{-1}) due to the alloying effect (Fig. 3b, Table S8). More importantly, as illustrated in Fig. 3c, the ORR Tafel slope of $Pt_{0.38}Cu_{0.62}$/N-HCS was only 50.66 mV dec^{-1}, much lower than those of commercial Pt/C (62.15 mV dec^{-1}), Pt/N-HCS (76.72 mV dec^{-1}) and $Pt_{0.38}Cu_{0.62}$/HCS (62.99 mV dec^{-1}), manifesting the promoted ORR kinetics on $Pt_{0.38}Cu_{0.62}$/N-HCS [47,48]. The ORR performance of the $Pt_{0.38}Cu_{0.62}$/HCS also surpassed those of most earlier reported Pt-based nanocatalysts (Fig. S21, Table S9).

A rotating ring-disk electrode (RRDE) was employed to investigate H_2O_2 yield and evaluate the electron transfer numbers for all catalysts (Fig. 3d) [49,50]. The $Pt_{0.38}Cu_{0.62}$/N-HCS catalyst displayed a four-electron ORR mechanism with an electron transfer numbers of 3.8 and a lower H_2O_2 production rate of 6%, which closely approached the value achieved by commercial Pt/C catalyst (n: ~3.85, H_2O_2: ~3%). This finding revealed that the $Pt_{0.38}Cu_{0.62}$/N-HCS catalyst exhibited a remarkable selectivity for direct reduction of O_2 to H_2O. The improved

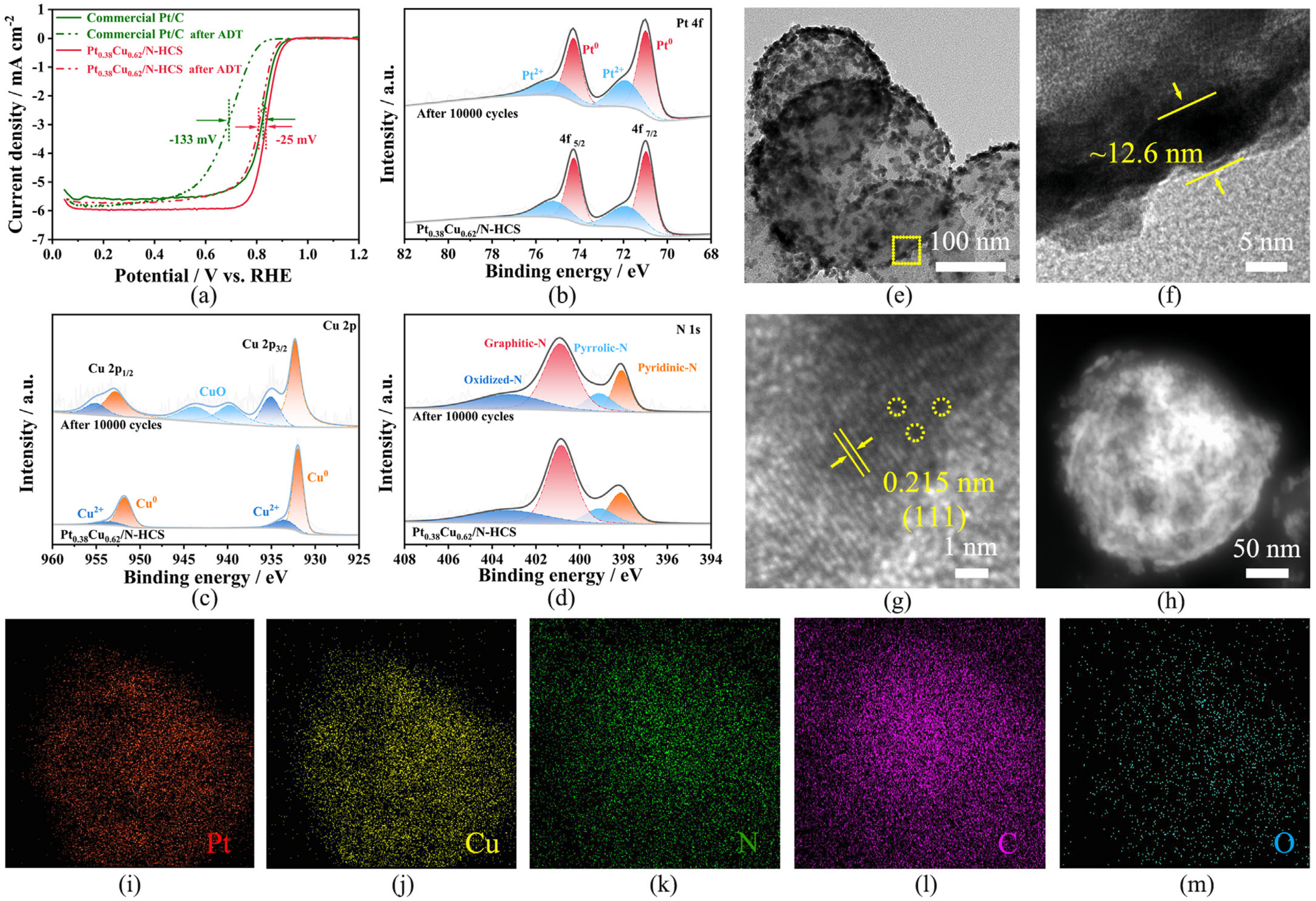

Fig. 5. (a) Comparison of LSV curves of $Pt_{0.38}Cu_{0.62}$/N-HCS and commercial Pt/C catalysts before and after stability test (10000 CV cycles in 0.1 M $HClO_4$), (b) Pt 4f fine spectrum, (c) Cu 2p fine spectrum, (d) N 1s fine spectrum before and after stability test of $Pt_{0.38}Cu_{0.62}$/N-HCS. (e) TEM, (f) yellow boxed portion of (e), (g) HR-TEM, (h-m) HAADF-STEM images and elemental mapping results after ADT of $Pt_{0.38}Cu_{0.62}$/N-HCS.

ORR kinetics was further confirmed by electrochemical impedance spectroscopy (EIS). Notably, as depicted in Fig. 3e and Fig. S22, the $Pt_{0.38}Cu_{0.62}$/N-HCS possessed the smallest charge transfer impedance (R_{ct}) of 13.33 Ω, relative to Pt/N-HCS (14.04 Ω), $Pt_{0.38}Cu_{0.62}$/HCS (22.59 Ω) and commercial Pt/C (71.94 Ω), which suggested that the exceptional compressive strain in Pt, achieved by alloying with Cu, facilitates faster electron transfer during the ORR process [51,52]. Besides catalytic activity, the tolerance of methanol crossover and durability were also crucial factors for the service life of a real fuel cell system and must be taken into consideration. It can be seen from Fig. 3f, when the 1 M methanol is introduced into electrolyte at 400 s, the ORR current density of other catalyst experienced a sharp decrease except for $Pt_{0.38}Cu_{0.62}$/N-HCS, demonstrating its superior tolerance against methanol crossover [53,54].

To further reveal the intrinsic mechanisms of the enhanced ORR activity by constructing PtCu alloy, DFT calculation were carried out to analyze the particular characteristics for $Pt_{0.38}Cu_{0.62}$ alloy. First, we calculated the *fcc* structure of Pt, Cu, and $Pt_{0.38}Cu_{0.62}$ alloy. As shown in Fig. S23, due to the radius mismatch between Pt and Cu ions, the Pt-Pt bonds became shorter (2.73 Å) in $Pt_{0.4}Cu_{0.6}$ than those (2.81 Å) of Pt metal, which is consistent with previous XRD analysis. For the reason that the O_2 adsorption behaviors significantly affect the ORR activities on catalytic surface, the charge density difference of O_2 adsorbed on different catalytic surfaces were calculated. As seen from Fig. 4a-c and S24, the amount of the transferred charge on PtCu (111) is larger than that on Pt (111), indicating that the enhanced O_2 adsorption ability by compress strain strategy for $Pt_{0.4}Cu_{0.6}$ alloy. The projected density of states (PDOS) of different catalytic surfaces (see Fig. 4d) were also presented to further probe the crucial role of compress strain in $Pt_{0.4}Cu_{0.6}$ alloy for efficient ORR performance. The obvious upshift of d band center (-1.85 eV) can be observed for $Pt_{0.4}Cu_{0.6}$ alloy relative to Pt (-2.11 eV) and Cu (-2.16 eV). A more positive value of d-band center would produce a decreased antibonding orbitals filling, which increases the interaction between the active metal sites and oxygen molecular. Therefore, the existence of compress strain could finally enhance the O_2 adsorption energy on PtCu (111) surface (see Fig. 4e). Finally, The Gibbs free energy diagrams for ORR with four-electrons pathway were calculated. As depicted in Fig. 4f-g, the fourth electron transfer step ($*OH + H^+ + e^- \rightarrow H_2O$) determines the potential-determining step (PDS) for Cu and Pt catalysts. Accordingly, Pt possesses a lower overpotential (0.31 eV) than those of Cu (0.97 eV). However, $Pt_{0.4}Cu_{0.6}$ alloy has a similar overpotential (0.33 eV) to pure Pt even though the first electron transfer step ($O_2 + H^+ + e^- \rightarrow *OOH$) is PDS, indicating that an efficient ORR activity for PtCu alloy with decreased Pt amount.

Accelerated durability test (ADT) was carried out by 10,000 CV cycles with a scan rate of 50 mV s^{-1} at a potential of 0.05-1.2 V (*vs.* RHE). Fig. 5a presented a comparative analysis of the LSV curves for both commercial Pt/C and $Pt_{0.38}Cu_{0.62}$/N-HCS catalysts before and after 10,000 cycles. The $E_{1/2}$ decay of $Pt_{0.38}Cu_{0.62}$/N-HCS exhibited no significantly different after 10,000 CV cycles when compared to its initial catalyst. In contrast, the commercial Pt/C catalyst experienced a substantial degradation with a notable negative shift of 133 mV in $E_{1/2}$. This outcome substantiates that the $Pt_{0.38}Cu_{0.62}$/N-HCS catalyst demonstrated outstanding durability during the ORR process, attributed to the stress effect induced by

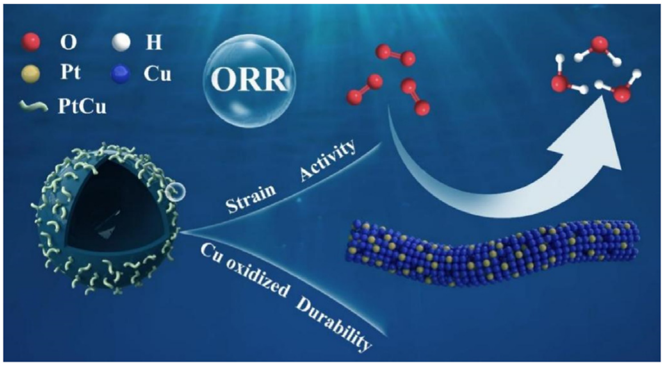

Fig. 6. The enhancement mechanism of $Pt_{0.38}Cu_{0.62}$/N-HCS catalyst towards ORR.

the alloy. In addition, the XRD plots (Fig. S25) analysis indicated that the materials still maintain the PtCu peak after ADT and no significant changes of XPS full spectrum. Pt 4f, Cu 2p, N 1s and C 1s XPS of $Pt_{0.38}Cu_{0.62}$/N-HCS before and after ADT were found (Fig. 5b-d, Fig. S26 and Fig. S27). One of these exhibits a distinct satellite peak at 937-947eV due to the oxidation of Cu on the surface [24]. According to most reports, commercial Pt/C lost a significant amount of Pt^0 after ADT, resulting in a rapid decline in electrochemical activity [55]. The compression stress caused by reasonable introduction of Cu atoms in Pt metal can effectively inhibit the conversion of Pt^0 to Pt^{2+}, resulting excellent durability of $Pt_{0.38}Cu_{0.62}$/N-HCS.

The morphology of $Pt_{0.38}Cu_{0.62}$/N-HCS (Fig. 5e) and the wall thickness of the support were well maintained (Fig. 5f). The d lattice spacing of 0.215 nm was obviously observed in HR-TEM image (Fig. 5g). The selected area electron diffraction (SAED) image of $Pt_{0.38}Cu_{0.62}$/N-HCS after ADT further confirmed that the PtCu alloy also remain *fcc* structure (Fig. S28). In addition, the elements of Pt, Cu, N, and C were uniformly distributed in the $Pt_{0.38}Cu_{0.62}$/N-HCS after ADT (Fig. 5h-m). The content of the O element had identified with respect to the before ADT, which suggested that there was an oxide generation during the ADT, which corresponds to the emergence of the Cu oxides from XPS (Fig. S29, Fig. S30, Table S10 and Table S11). The preferential oxidation of Cu better protects Pt^0, which was the main reason for the stable performance of $Pt_{0.38}Cu_{0.62}$/N-HCS.

Based on the above discussion, the superior ORR performance of the $Pt_{0.38}Cu_{0.62}$/N-HCS catalyst can be attributed to the three main factors. Firstly, the incorporating Cu atoms with a smaller atomic radius into the Pt lattice decreases the length of Pt-Pt bonds and induces compressive strain in the PtCu nanoalloy. This modification effectively shifts the d band center of Pt approaching the Fermi level, resulting in increased adsorption energy toward O_2 molecules and ultimately enhancing the ORR activity. Secondly, the Cu atoms acts as sacrificial anode and undergo preferential oxidation when compared to Pt. This selective oxidation protects the highly active sites of Pt and the functional carbon support from corrosion, thereby improving the durability; Finally, the stable Cu species present in the PtCu alloys play a significant role in maintaining the strain effect, ensuring the continued enhancement of both activity and durability of the catalyst (Fig. 6).

3. Conclusion

In summary, we have successfully prepared a worm-liked PtCu nanocrystals loaded on nitrogen-doped carbon hollow microspheres ($Pt_{0.38}Cu_{0.62}$/N-HCS). The unique structure of N-HCS, featuring a defined hollow sphere with a thin and mesoporous shell, effectively prevents PtCu alloy aggregation. Furthermore, the strong compressive strain between Pt and Cu atoms modifies the electron transfer from Cu to Pt surface and optimizes the electronic configuration of Pt. These structural and compositional advantages contribute to the superior performance of $Pt_{0.38}Cu_{0.62}$/N-HCS catalyst compared to commercial Pt/C catalyst. The $Pt_{0.38}Cu_{0.62}$/N-HCS catalyst demonstrates higher $E_{1/2}$, mass activity, ECSA, and tolerance against methanol crossover. Moreover, the $Pt_{0.38}Cu_{0.62}$/N-HCS catalyst also exhibits faster reaction kinetic and rapid interfacial charge transfer. It also shows remarkable durability, as evidenced by only a small negative shift of 25 mV in $E_{1/2}$ after 10,000 cycles. Theoretical calculations and experiment studies further reveals that the superior ORR activity and stability result from the optimized electronic structures of Pt induced by the strain effect, as well as the protective effect of preferential oxidation of Cu on Pt corrosion. This work presents a novel strategy for designing and preparing highly effective and stable PtM alloy catalysts for ORR.

Declaration of competing interest

The authors declare no conflict of interest.

Acknowledgements

This research was funded by the Young Elite Scientists Sponsorship Program by CAST (2021QNRC001), Natural Science Foundation of Chongqing (CSTB2022NSCQ-MSX0557, cstb2023nscq-msx0979), Talent Introduction of Chongqing University of Science and Technology (ckrc2021050, ckrc20230401, ckrc2021053), the Science and Technology Research Program of Chongqing Municipal Education Commission (KJQN202201532, KJQN202301542), the National Natural Science Foundation of China (22109016) and Open Research Fund of CNMGE Platform & NSCC-TJ (CNMGE2023016). Thanks Hong He for the help in the test of XRD and Liang Yan from Shiyanjia Lab (http://www.shiyanjia.com) for XPS and ICP tests.

Appendix A. Supplementary data

Supplementary data to this article can be found online at https://doi.org/10.1016/j.nanoms.2024.02.011.

References

[1] R. Anahara, S. Yokokawa, M. Sakurai, Present status and future prospects for fuel cell power systems, Proc. IEEE 81 (1993) 399–408.
[2] X. Tian, X.F. Lu, B.Y. Xia, X.W. Lou, Advanced electrocatalysts for the oxygen reduction reaction in energy conversion technologies, Joule 4 (2020) 45–68.
[3] L. Ding, T. Tang, J.-S. Hu, Recent progress in proton-exchange membrane fuel cells based on metal-nitrogen-carbon catalysts, Acta Phys. Chim. Sin. 37 (2020) 2010048.
[4] M. Bao, I.S. Amiinu, T. Peng, W. Li, S. Liu, Z. Wang, Z. Pu, D. He, Y. Xiong, S. Mu, Surface evolution of PtCu alloy shell over Pd nanocrystals leads to superior hydrogen evolution and oxygen reduction reactions, ACS Energy Lett. 3 (2018) 940–945.
[5] S.-Y. Lu, B. Huang, M. Sun, M. Luo, M. Jin, H. Yang, Q. Zhang, H. Liu, P. Zhou, Y. Chao, K. Yin, C. Shang, J. Wang, Y. Wang, F. Lv, L. Gu, S. Guo, Synthetic tuning stabilizes a high-valence Ru single site for efficient electrolysis, Nat. Synth. (2023).
[6] W. Zhang, P. Li, H. Zhao, L. Zong, L. Wang, Metal-free honeycomb-like electrocatalyst with high specific mass activity for accelerated oxygen reduction reaction in both alkaline and acidic media, Appl. Surf. Sci. 579 (2022) 152149.
[7] L. Huang, S. Zaman, Z. Wang, H. Niu, B. You, B. Yu Xia, Synthesis and application of platinum-based hollow nanoframes for direct alcohol fuel cells, Acta Phys. Chim. Sin. 37 (2021) 2009035.
[8] M. Jin, R. Wang, B. Jia, J. Zhang, H. Liu, S.-Y. Lu, Achieving uniform Pt deposition site by tuning the surface microenvironment of bamboo-like carbon nanotubes, Appl. Surf. Sci. 591 (2022) 153201.
[9] M. Jin, S.-Y. Lu, X. Zhong, H. Liu, H. Liu, M. Gan, L. Ma, Spindle-like MOF derived TiO_2@ NC–NCNTs composite with modulating defect site and graphitization nanoconfined Pt NPs as superior bifunctional fuel cell electrocatalysts, ACS Sustain. Chem. Eng. 8 (2020) 1933–1942.
[10] R. Shen, W. Chen, Q. Peng, S. Lu, L. Zheng, X. Cao, Y. Wang, W. Zhu, J. Zhang, Z. Zhuang, C. Chen, D. Wang, Y. Li, High-concentration single atomic Pt sites on hollow CuSx for selective O_2 reduction to H_2O_2 in acid solution, Chem 5 (2019) 2099–2110.
[11] Y. Nakaya, S. Furukawa, Catalysis of alloys: classification, principles, and design for a variety of materials and reactions, Chem. Rev. 123 (2022) 5859–5947.
[12] S. Zhang, S. Liu, J. Huang, H. Zhou, X. Liu, P. Tan, H. Chen, Y. Liang, J. Pan, Microbial synthesis of N, P co-doped carbon supported PtCu catalysts for oxygen reduction reaction, J. Energy Chem. 84 (2023) 486–495.

[13] Y. Wu, L. Chen, S. Geng, Y. Tian, R. Chen, K. Wang, Y. Wang, S. Song, PtFe nanoalloys supported on Fe-based cubic framework as efficient oxygen reduction electrocatalysts for proton exchange membrane fuel cells, Adv. Funct. Mater. 34 (2023) 2307297.

[14] M. Zhang, T. Zhou, D. Bukhvalov, F. Han, C. Wang, X. Yang, Metal-support interaction promoted multifunctional electrocatalysis on PtCo/NC with ultralow Pt loading for oxygen reduction reaction and zinc-air battery, Appl. Catal., B 337 (2023) 122976.

[15] W. Yan, O. Guo, Q. Xing, M. Liao, Z. Shi, H. Feng, Y. Zhang, X. Li, Y. Chen, Atomically dispersed Ni–N_4 sites assist Pt_3Ni nanocages with Pt skin to synergistically enhance oxygen reduction activity and stability, Small 19 (2023) 2300200.

[16] W. Li, Z.-Y. Hu, Z. Zhang, P. Wei, J. Zhang, Z. Pu, J. Zhu, D. He, S. Mu, G. Van Tendeloo, Nano-single crystal coalesced PtCu nanospheres as robust bifunctional catalyst for hydrogen evolution and oxygen reduction reactions, J. Catal. 375 (2019) 164–170.

[17] X. Luo, C. Fu, S. Shen, L. Luo, J. Zhang, Free–templated synthesis of N–doped PtCu porous hollow nanospheres for efficient ethanol oxidation and oxygen reduction reactions, Appl. Catal., B 330 (2023) 122602.

[18] X. Liu, Q. Xing, J. Song, Z. Xiao, F. Wang, T. Yang, J. Yu, W. Chen, X. Li, Y. Chen, A facile strategy to prepare FeNx decorated PtFe intermetallic with excellent acidic oxygen reduction reaction activity and stability, J. Colloid Interface Sci. 645 (2023) 241–250.

[19] S. Hu, Z.-A. Li, Facile synthesis of PtCo nanoparticles/three-dimensional graphene hybrid material as a highly active and stable electrocatalyst for oxygen reduction reaction, Chem. Eng. J. 471 (2023) 144828.

[20] M. Luo, S. Guo, Strain-controlled electrocatalysis on multimetallic nanomaterials, Nat. Rev. Mater. 2 (2017) 17059.

[21] J.C. Meier, C. Galeano, I. Katsounaros, A.A. Topalov, A. Kostka, F. Schüth, K.J.J. Mayrhofer, Degradation mechanisms of Pt/C fuel cell catalysts under simulated start–stop conditions, ACS Catal. 2 (2012) 832–843.

[22] F.J. Perez-Alonso, C.F. Elkjær, S.S. Shim, B.L. Abrams, I.E.L. Stephens, I. Chorkendorff, Identical locations transmission electron microscopy study of Pt/C electrocatalyst degradation during oxygen reduction reaction, J. Power Sources 196 (2011) 6085–6091.

[23] Y. Wang, C. Han, P. Xie, H. Li, P. Yao, J. Cao, M. Ruan, P. Song, X. Gong, M. Lu, W. Xu, Highly dispersed PtNi nanoparticles modified carbon black as high-performance electrocatalyst for oxygen reduction in acidic medium, J. Electroanal. Chem. 904 (2022) 115908.

[24] F. Xu, S. Cai, B. Lin, L. Yang, H. Le, S. Mu, Geometric engineering of porous PtCu nanotubes with ultrahigh methanol oxidation and oxygen reduction capability, Small 18 (2022) 2107387.

[25] B.Y. Xia, W.T. Ng, H.B. Wu, X. Wang, X.W. Lou, Self-Supported interconnected Pt nanoassemblies as highly stable electrocatalysts for low-temperature fuel cells, Angew. Chem. Int. Ed. 51 (2012) 7213–7216.

[26] Y. Hu, X. Guo, T. Shen, Y. Zhu, D. Wang, Hollow porous carbon-confined atomically ordered $PtCo_3$ intermetallics for an efficient oxygen reduction reaction, ACS Catal. 12 (2022) 5380–5387.

[27] F. Su, Z. Tian, C.K. Poh, Z. Wang, S.H. Lim, Z. Liu, J. Lin, Pt nanoparticles supported on nitrogen-doped porous carbon nanospheres as an electrocatalyst for fuel cells, Chem. Mater. 22 (2009) 832–839.

[28] C. Wang, L. Kuai, W. Cao, H. Singh, A. Zakharov, Y. Niu, H. Sun, B. Geng, Highly dispersed Cu atoms in MOF-derived N-doped porous carbon inducing Pt loads for superior oxygen reduction and hydrogen evolution, Chem. Eng. J. 426 (2021) 130749.

[29] X. Xu, C. Xu, J. Liu, R. Jin, X. Luo, C. Shu, H. Chen, C. Guo, L. Xu, Y. Si, The synergistic effect of "soft-hard template" to in situ regulate mass transfer and defective sites of doped-carbon nanostructures for catalysis of oxygen reduction, J. Alloys Compd. 939 (2023) 168782.

[30] X. Chen, K. Niu, Z. Xue, X. Liu, B. Liu, B. Zhang, H. Zeng, W. Lv, Y. Zhang, Y. Wu, Ultrafine platinum nanoparticles supported on N,S-codoped porous carbon nanofibers as efficient multifunctional materials for noticeable oxygen reduction reaction and water splitting performance, Nanoscale Adv. 4 (2022) 1639–1648.

[31] J. Garcia-Cardona, F. Alcaide, E. Brillas, I. Sirés, P.L. Cabot, Testing PtCu nanoparticles supported on highly ordered mesoporous carbons CMK3 and CMK8 as catalysts for low-temperature fuel cells, Catalysts 11 (2021) 724.

[32] B. Li, Y. Ren, C. Lv, F. Gao, X. Zhang, X. Yang, L. Li, Z. Lu, X. Yu, Synthesis of ultrathin-wall PtCu nanocages as efficient electrocatalyst toward oxygen reduction reactivity, Int. J. Hydrogen Energy 48 (2023) 16286–16293.

[33] X. Zhang, Z. An, Z. Xia, H. Li, X. Xu, S. Yu, S. Wang, G. Sun, Phosphoric acid resistance PtCu/C oxygen reduction reaction electrocatalyst for HT-PEMFCs: a theoretical and experimental study, Appl. Surf. Sci. 619 (2023) 156663.

[34] K. Zhao, T. Qian, X. Bai, M. Feng, H. Gao, T. Xia, Z. Wang, H. Guo, PtNi multi-branched nanostructures as efficient bifunctional electrocatalysts for fuel cell, J. Phys. D Appl. Phys. 55 (2022) 344001.

[35] K. Ramachandran, M. Vinothkannan, A.R. Kim, S. Ramakrishnan, D.J. Yoo, Ultrafine bimetallic alloy supported on nitrogen doped reduced graphene oxide toward liquid-fuel oxidation: profile of improved performance and extended durability, Int. J. Hydrogen Energy 44 (2019) 21769–21780.

[36] L. Zhao, J. Jiang, S. Xiao, Z. Li, J. Wang, X. Wei, Q. Kong, J.S. Chen, R. Wu, PtZn nanoparticles supported on porous nitrogen-doped carbon nanofibers as highly stable electrocatalysts for oxygen reduction reaction, Nano Mater. Sci. 5 (2023) 329–334.

[37] T. Song, H. Xue, J. Sun, N. Guo, J. Sun, Q. Wang, Solvent assistance induced surface N-modification of PtCu aerogels and their enhanced electrocatalytic properties, Chem 57 (2021) 7140–7143.

[38] S. Li, H. Sun, J. Zhang, L. Zheng, Y. Li, X. Fang, Y. Liu, Q. Song, Z. Wang, Y. Gao, X. Zhang, X. Dai, Y. Cai, F. Gao, Interfacial synergistic effect in SnO_2/PtNi nanocrystals enclosed by high-index facets for high-efficiency ethylene glycol electrooxidation, Nano Res. 15 (2022) 7877–7886.

[39] B. Wu, J. Xiao, L. Li, T. Hu, M. Qiu, D. Lützenkirchen-Hecht, K. Yuan, Y. Chen, Arranging electronic localization of PtCu nanoalloys to stimulate improved oxygen electroreduction for high-performance fuel cells, CCS Chem. 5 (2023) 2545–2556.

[40] Q. Shu, J. Zhang, B. Hu, X. Deng, J. Yuan, R. Ran, W. Zhou, Z. Shao, Rational design of a high-durability Pt-based ORR catalyst supported on Mn/N codoped carbon sheets for PEMFCs, Energy Fuels 36 (2022) 1707–1715.

[41] M. Gong, D. Xiao, Z. Deng, R. Zhang, W. Xia, T. Zhao, X. Liu, T. Shen, Y. Hu, Y. Lu, X. Zhao, H. Xin, D. Wang, Structure evolution of PtCu nanoframes from disordered to ordered for the oxygen reduction reaction, Appl. Catal., B 282 (2021) 119617.

[42] N. Guo, H. Xue, A. Bao, Z. Wang, J. Sun, T. Song, X. Ge, W. Zhang, K. Huang, F. He, Q. Wang, Achieving superior electrocatalytic performance by surface copper vacancy defects during electrochemical etching process, Angew. Chem. Int. Ed. 59 (2020) 13778–13784.

[43] H. Jin, Z. Kou, W. Cai, H. Zhou, P. Ji, B. Liu, A. Radwan, D. He, S. Mu, P–Fe bond oxygen reduction catalysts toward high-efficiency metal–air batteries and fuel cells, J. Mater. Chem. A 8 (2020) 9121–9127.

[44] M. Liu, X. Yin, X. Guo, L. Hu, H. Yuan, G. Wang, F. Wang, L. Chen, L. Zhang, F. Yu, High efficient oxygen reduction performance of Fe/Fe_3C nanoparticles in situ encapsulated in nitrogen-doped carbon via a novel microwave-assisted carbon bath method, Nano Mater. Sci. 1 (2019) 131–136.

[45] S.-Y. Lu, W. Dou, J. Zhang, L. Wang, C. Wu, H. Yi, R. Wang, M. Jin, Amorphous-crystalline interfaces coupling of CrS/CoS_2 few-layer heterojunction with optimized crystallinity boosted for water-splitting and methanol-assisted energy-saving hydrogen production, Acta Phys. Chim. Sin. 40 (2024) 2308024.

[46] W.-J. Lee, S. Bera, H.-J. Woo, W. Hong, J.-Y. Park, S.-J. Oh, S.-H. Kwon, Atomic layer deposition enabled PtNi alloy catalysts for accelerated fuel-cell oxygen reduction activity and stability, Chem. Eng. J. 442 (2022) 136123.

[47] Y. Jiao, X. Gu, P. Zhai, Y. Wei, W. Liu, Q. Chen, Z. Yang, J. Zuo, L. Wang, T. Xu, Y. Gong, Three-dimensional Fe single-atom catalyst for high-performance cathode of Zn–air batteries, Nano Lett. 22 (2022) 7386–7393.

[48] G. Wang, Z. Yang, Y. Du, Y. Yang, Programmable exposure of Pt active facets for efficient oxygen reduction, Angew. Chem. Int. Ed. 58 (2019) 15848–15854.

[49] W.-Z. Li, B.-A. Lu, L. Gan, N. Tian, P.-Y. Zhang, W. Yan, W.-X. Chen, Y.-H. Chen, Z.-Y. Zhou, S.-G. Sun, High activity and durability of carbon-supported core-shell PtP_x@Pt/C catalyst for oxygen reduction reaction, Chin. J. Catal. 42 (2021) 2173–2180.

[50] T. Song, H. Xue, N. Guo, J. Sun, L. Qin, L. Guo, K. Huang, F. He, Q. Wang, Dual-modulation of electronic structure and active sites of PtCu nanodendrites by surface nitridation to achieve efficient methanol electrooxidation and oxygen reduction reaction, Chem 56 (2020) 7136–7139.

[51] D. Mladenović, D.M.F. Santos, G. Bozkurt, G.S.P. Soylu, A.B. Yurtcan, Š. Miljanić, B. Šljukić, Tailoring metal-oxide-supported PtNi as bifunctional catalysts of superior activity and stability for unitised regenerative fuel cell applications, Electrochem. Commun. 124 (2021) 106963.

[52] Z. Zhang, C. Liu, Y. Dai, B. Liu, P. Guo, F. Tu, M. Ma, L. Shen, Z. Zhao, Y. Liu, Y. Zhang, L. Zhao, Z. Wang, Sandwich-structured MXene/carbon hybrid support decorated with Pt nanoparticles for oxygen reduction reaction, ACS Appl. Energy Mater. 5 (2022) 14957–14965.

[53] X. Chen, J. Guo, J. Liu, Z. Luo, X. Zhang, D. Qian, D. Sun-Waterhouse, G.I.N. Waterhouse, Nanostructure engineering and electronic modulation of a PtNi alloy catalyst for enhanced oxygen reduction electrocatalysis in zinc–air batteries, J. Phys. Chem. Lett. 14 (2023) 1740–1747.

[54] W. Ye, Z. Wu, S. Zhang, Y. Sun, X. Zhang, W. Zhou, W. Cao, T. Wang, D. Cheng, H. Xie, PtNi alloy nanoparticles grown in situ on nitrogen doped carbon for the efficient oxygen reduction reaction, Dalton Trans. 52 (2023) 10817–10827.

[55] M. Chen, F. Kong, H. Yao, Y. Chen, G. Meng, Z. Chang, C. Chen, H. Tian, L. Wang, X. Cui, J. Shi, Dual metal-organic frameworks-derived Fe-atomic sites bounded to fine Fe/Fe_xC nanoparticles for enhanced oxygen electroreduction, Chem. Eng. J. 453 (2023) 139820.